

Gigahertz Electromagnetic Structures via Direct Ink Writing for Radio-Frequency Oscillator and Transmitter Applications

Nanjia Zhou, Chengye Liu, Jennifer A. Lewis,* and Donhee Ham*

Radio-frequency (RF) electronics, which combine passive electromagnetic devices and active transistors to generate and process gigahertz (GHz) signals, provide a critical basis of ever-pervasive wireless networks. While transistors are best realized by top-down fabrication, relatively larger electromagnetic passives are within the reach of printing techniques. Here, direct writing of viscoelastic silver-nanoparticle inks is used to produce a broad array of RF passives operating up to 45 GHz. These include lumped devices such as inductors and capacitors, and wave-based devices such as transmission lines, their resonant networks, and antennas. Moreover, to demonstrate the utility of these printed RF passive structures in active RF electronic circuits, they are combined with discrete transistors to fabricate GHz self-sustained oscillators and synchronized oscillator arrays that provide RF references, and wireless transmitters clocked by the oscillators. This work demonstrates the synergy of direct ink writing and RF electronics for wireless applications.

Wireless technology has undergone a profound transformation from cellular voice communications to pervasive networks that connect humans, machines, and “things” with ever increasing data content and capacity. Central to this wireless revolution are chip-scale radio-frequency (RF) electronics that combine passive electromagnetic devices and active transistors to generate and process gigahertz (GHz) signals. While transistors are best realized by top-down fabrication, relatively larger electromagnetic passives are within the reach of printing techniques. To date, inkjet printing,^[1–6] screen printing,^[7–11] and roll-to-roll printing^[12] have been widely investigated for patterning planar electromagnetic passives. 3D printing offers another approach for creating RF passive devices, with the potential to expand their functional diversity through tailoring their structure in 3D space. Several 3D printing methods,^[13] including material extrusion,^[14–20] material jetting,^[21] power-bed fusion,^[22,23] and vat photopolymerization,^[24] have been used to make RF

passives, such as antennas,^[17,18,23,24] lenses,^[19,20] and waveguides,^[21,22] with different materials and size scales.

Of these 3D printing methods, extrusion-based direct writing of viscoelastic silver-nanoparticle inks^[14–18] is well suited for fabricating chip-scale RF passives due to their fine feature resolution of $\approx 10 \mu\text{m}$ or below. Although printed and thermally annealed silver traces have 3–6 times higher resistivity, ρ , than bulk silver,^[14,17] this does not pose a fundamental barrier to RF applications since their RF resistance, which is proportional to $\sqrt{\rho}$ due to the skin effect, is only 1.7–2.4 times higher. To date, direct ink writing has been used to fabricate electrically small antennas composed of conductive meander lines printed on a glass hemispherical substrates^[17] and simple coil antennas for bioelectronics.^[18]

However, the potential for creating a far greater set of RF passive devices via direct ink writing as well as their integration into active RF electronic circuits has yet to be explored.

Here, we produce a broad array of RF passives that operate at GHz frequencies via direct ink writing, including lumped devices (e.g., inductors and capacitors) and wave-based devices (e.g., transmission lines, their resonant networks, and antennas), whose maximum quality factors (Q) and operational frequencies exceed 40 and 45 GHz, respectively. Moreover, to demonstrate the utility of these printed RF passive structures in active RF electronic circuits, we combine them with discrete transistors to fabricate self-sustained oscillators, synchronized oscillator arrays, and wireless transmitters clocked by the oscillators. We specifically focus on autonomous oscillators, given their crucial role in providing radio frequency references for virtually all wireless devices.

Figure 1a–f (and Figure S1 and S3–S5 in the Supporting Information) shows the broad palette of GHz passive electromagnetic structures created by direct writing of a viscoelastic silver ink (see Experimental Section). They are designed using an electromagnetic field solver (Figure S6–S8, Supporting Information) and printed by extruding this ink through fine deposition nozzles with diameters of 10 or 50 μm (Movie S1–S3, Supporting Information) on glass (Figure 1; Figure S1 and S3, Supporting Information) or polyimide substrates (Figure S4 and S5, Supporting Information).^[14] The width of the printed and thermally annealed (300 °C for 30 min) silver features is nearly equivalent to the nozzle diameter used, while their thickness is 60–80% of the nozzle diameter when printed on a substrate and is approximately the same as the nozzle diameter when printed out of plane (in air). After heat treatment,

Dr. N. Zhou, Prof. J. A. Lewis
Wyss Institute for Biologically Inspired Engineering
John A. Paulson School of Engineering
and Applied Sciences
Harvard University
Cambridge, MA 02138, USA
E-mail: jalewis@seas.harvard.edu



C. Liu, Prof. D. Ham
John A. Paulson School of Engineering and Applied Sciences
Harvard University
Cambridge, MA 02138, USA
E-mail: donhee@seas.harvard.edu

DOI: 10.1002/adma.201605198

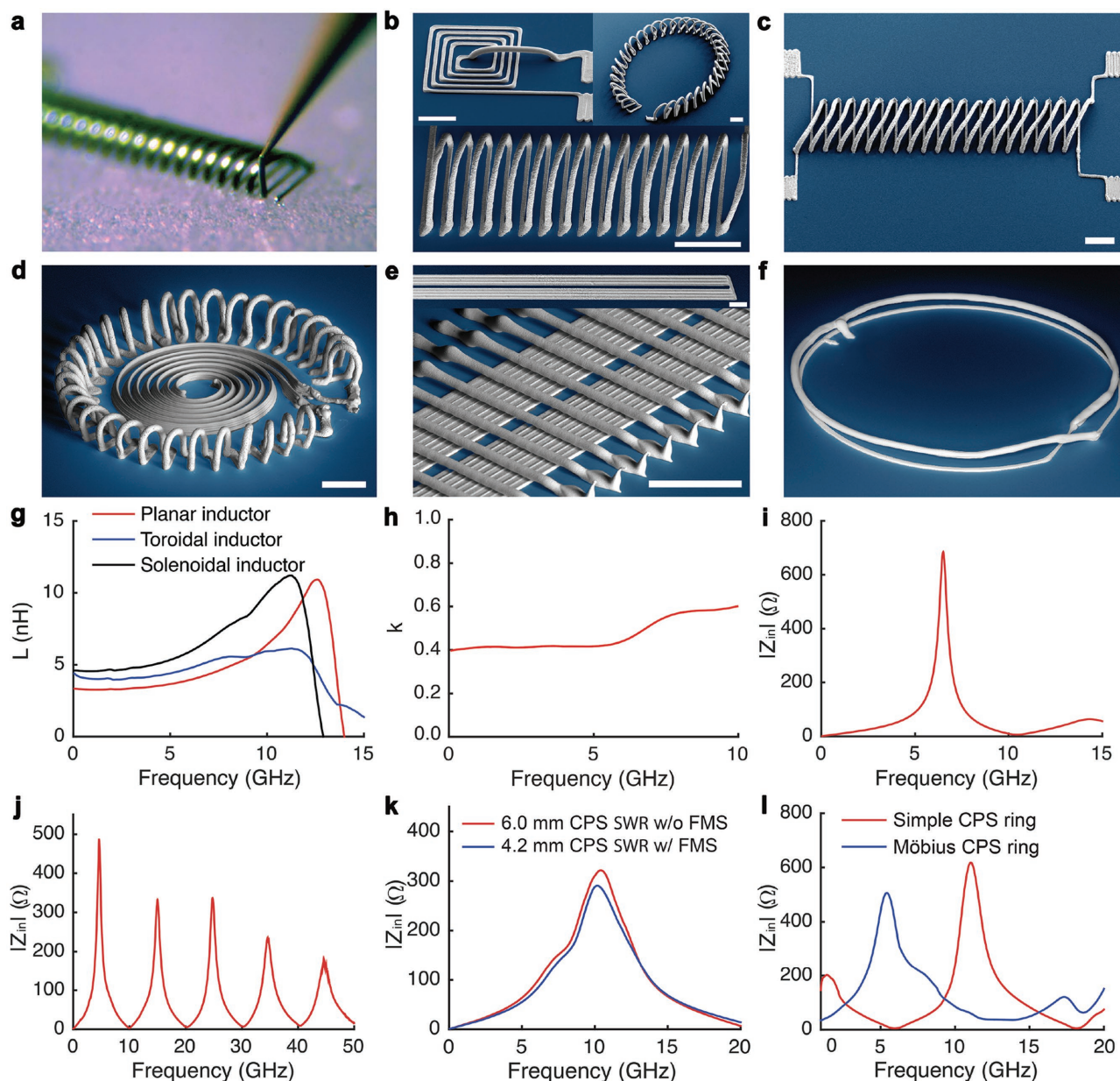


Figure 1. 3D printed passive devices on glass substrates and their measured RF characteristics. a) Direct writing of a viscoelastic silver ink through at 10 μm nozzle. b) Top left: A 4-turn planar inductor; top right: a 33-turn toroidal inductor; bottom: a 16-turn solenoidal inductor. c) 1:1 solenoidal transformer. d) LC resonator consisting of a 32-turn toroidal inductor and a parallel-plate capacitor. e) FMS-free and FMS-loaded CPS SWRs. f) Möbius CPS ring (diameter: 5 mm). g) L of the inductors of part (b). h) Coupling coefficient of the transformer of part (c). i) Magnitude of input impedance Z_{in} of the LC resonator of part (d). j) $|Z_{in}|$ of a 13.4 mm long CPS SWR. k) $|Z_{in}|$ of FMS-free and FMS-loaded CPS SWRs with differing lengths. l) $|Z_{in}|$ of Möbius and simple CPS rings (diameter: 5 mm). All scale bars are 100 μm . [Note: The geometric parameters of these devices are provided in Figure S1 in the Supporting Information.]

ρ of the conductive traces is $\approx 1 \times 10^{-5} \Omega \text{ cm}$,^[14] and thus, their DC and RF resistances per unit cross-sectional area are ≈ 6 and ≈ 2.4 times higher than those of bulk silver. To characterize their RF properties, we carry out microwave scattering experiments (Figure 1g–l; Experimental Section and Figure S2 in the Supporting Information).

The inductance L of representative planar, solenoidal, and toroidal inductors (Figure 1b) as a function of frequency shows a self-resonance frequency f_s in excess of 10 GHz (Figure 1g),

i.e., they function as intended inductors well into the GHz regime. These inductors exhibit a maximum quality factor Q in excess of 40 (Figure S1, Supporting Information), which is on a par with the Q values of commercially available inductors of various implementations. This performance is achieved by compensating the increased per-unit-area RF resistance of the silver-nanoparticle ink with greater trace thickness. While the planar and solenoidal inductors on glass substrate (Figure 1b) exhibit similar Q values, the solenoidal inductor has a higher Q

than the planar inductor when they are implemented on a conductive substrate such as silicon (Figure S9, Supporting Information). In this case, 3D structuring is advantageous, because the magnetic field in the solenoidal structure is largely parallel to the substrate, which reduces the lossy eddy current in the conductive substrate.

Direct ink writing is also used to print RF passive networks that combine multiple elements. For example, two identical solenoids interpenetrating each other form a 1:1 transformer (Figure 1c), whose mutual inductance is 41% of the self-inductance of either solenoid (Figure 1h). In another example, we printed a toroidal inductor and a parallel-plate capacitor in shunt to produce an LC resonator (Figure 1d) that exhibits a Q of 10 and a resonance frequency f_R of 6.5 GHz (Figure 1i). In this embodiment, the parallel-plate capacitor is composed of two high-aspect-ratio walls with a distance of 10 μm between the two walls (Figure S1, Supporting Information).

To go beyond lumped passive electromagnetic structures, we created passive structures that exploit the full wave nature of electromagnetic energy propagation. As the first demonstration, we fabricated a transmission line in the form of coplanar strip (CPS) by printing two silver conductor lines in parallel (Figure 1e, top; conductor width $w = 70 \mu\text{m}$, thickness $t = 6\text{--}8 \mu\text{m}$, conductor-conductor spacing $s = 20 \mu\text{m}$, CPS length l : variable) and short-circuit its one end by connecting the two conductors at that end with a silver interconnect. A quasi-transverse electromagnetic (TEM) wave injected from the other, open, end of the CPS is reflected at the short end, and the superposition of these forward and reverse waves creates standing waves if l equals a quarter wavelength ($\lambda/4$) or its integer multiples. This frequency-selective formation of standing waves corresponds to resonance.^[25] For $l = 13.4 \text{ mm}$, the CPS standing wave resonator (SWR) clearly exhibits a fundamental resonance mode ($l = \lambda/4$) at 4.6 GHz, where the magnitude of the CPS input impedance, $|Z_{\text{in}}|$, becomes maximum, and higher harmonic resonance modes ($l = n \times \lambda/4$, $n = 2, 3, 4, \dots$) where $|Z_{\text{in}}|$ assumes local minima for even n and local maxima for odd n (Figure 1j). Within the measurement frequency range, the highest resonance peak frequency is at 44.6 GHz, which corresponds to the ninth harmonic (see Figure S10 in the Supporting Information for detailed harmonic analysis and influence of nonidealities). These data confirm the full wave nature of the printed device. The same pattern of multimode resonance emerges again for $l = 6.0 \text{ mm}$, with a fundamental mode at 10.4 GHz (Figure 1k, red; Figure S10, Supporting Information). From the fundamental harmonic modes, we estimate the quasi-TEM wave velocity v on these CPSs to be $v \approx 0.83 c$ (c is the speed of light in vacuum).

Miniaturization of passive devices is an important aspect of RF electronics, since they are far larger than transistors and thus typically define the overall system size. We first demonstrate passive device miniaturization by printing additive structures to a CPS SWR. Specifically, we printed an array of 80 floating metal strips (FMSs) above the CPS SWR (Figure 1e, bottom; interstrip distance: 40 μm ; $\approx 3\text{--}5 \mu\text{m}$ above the CPS; see also Figure S11 in the Supporting Information). This configuration lowers the wave velocity to $v \approx 0.58 c$ from $v \approx 0.83 c$, hence its wavelength by the same proportion.^[25] Thus, to attain a $\lambda/4$ standing wave resonance at a given frequency, the FMS-loaded

structure requires a shorter length than the FMS-free structure. Indeed, an FMS-loaded 4.2 mm long CPS SWR and an FMS-free 6 mm long CPS SWR exhibit the same fundamental resonance frequency of 10.4 GHz (Figure 1k).

The miniaturization strategy described above is based on wave slowing via 3D printing of peripheral structures around a given CPS structure. Another strategy is to change the CPS structure itself to alter the boundary condition, while maintaining the wave velocity. We highlight this by comparing the RF characteristics of a Möbius CPS ring (Figure 1f) to a simple CPS ring (Figure S3, Supporting Information). Each ring supports only those waves that have the same phase after looping around the ring once; that is, they exhibit resonance according to the periodic boundary condition. For the simple CPS ring, the periodic boundary condition is met when the ring perimeter equals λ (or its integer multiples),^[26] whereas in the Möbius CPS ring, it is met when the ring perimeter equals $\lambda/2$ (or its odd integer multiples).^[27] Hence, the perimeter of the Möbius CPS ring is half of that of the simple CPS ring for the same resonance frequency. In measurements of simple and Möbius CPS rings with the same diameter of 5 mm (Figure 1l), the 5.5 GHz resonance frequency of the Möbius ring is half of that of the simple ring, as expected; this translates to a 75% area reduction achieved by the Möbius twist.

To determine device reproducibility and mechanical robustness, we printed 20 identical solenoidal inductors in a single pass (Figure S12, Supporting Information). The overall yield is 75%, with 15 inductors exhibiting inductance values of $6.93 \pm 0.164 \text{ nH}$, in good agreement with the target inductance of 7 nH at 5 GHz. The other five inductors possessed shorted features, which reduce their effective number of turns, and, hence, their inductance values (>10%) below the target value. To assess their mechanical robustness, we subjected all 20 inductors to a vibration test (3000 rpm for $\approx 12 \text{ h}$) and then measured their inductance again (Figure S12, Supporting Information). For each inductor, the measured change in inductance is less than 0.5%, which is below the calibration error of the network analyzer. We anticipate that other printed passive devices, e.g., the FMS-loaded CPS and the Möbius CPS rings, would exhibit similar behavior.

Next, we demonstrate the heterogeneous integration of these printed RF passives with discrete transistors (Figure 2 and 3) to form self-sustained oscillators, where the transistors provide gain to compensate the resonator loss. We first create an oscillator in Colpitts topology (Figure 2a) on a glass substrate by first printing an LC resonator (consisting of one solenoidal inductor and two parallel-plate capacitors), resistors, and interconnects with the silver-nanoparticle ink, and then place a silicon germanium n-p-n bipolar junction transistor (Infineon BFR840L-3RHESD) with a footprint of 1 mm \times 0.6 mm. The oscillator is designed using a circuit simulator and an electromagnetic field solver (see Figure S13 in the Supporting Information). To pick and place the transistor, an empty nozzle (200 μm diameter) is mounted on the 3D printer and pneumatically pressurized in reverse to generate a modest suction pressure (18 psi). The transistor is then manually rotated with the nozzle and subsequently placed into the desired location such that the emitter, base, and collector pins of the transistor connect to three printed pads that provide both adhesion and electrical contacts

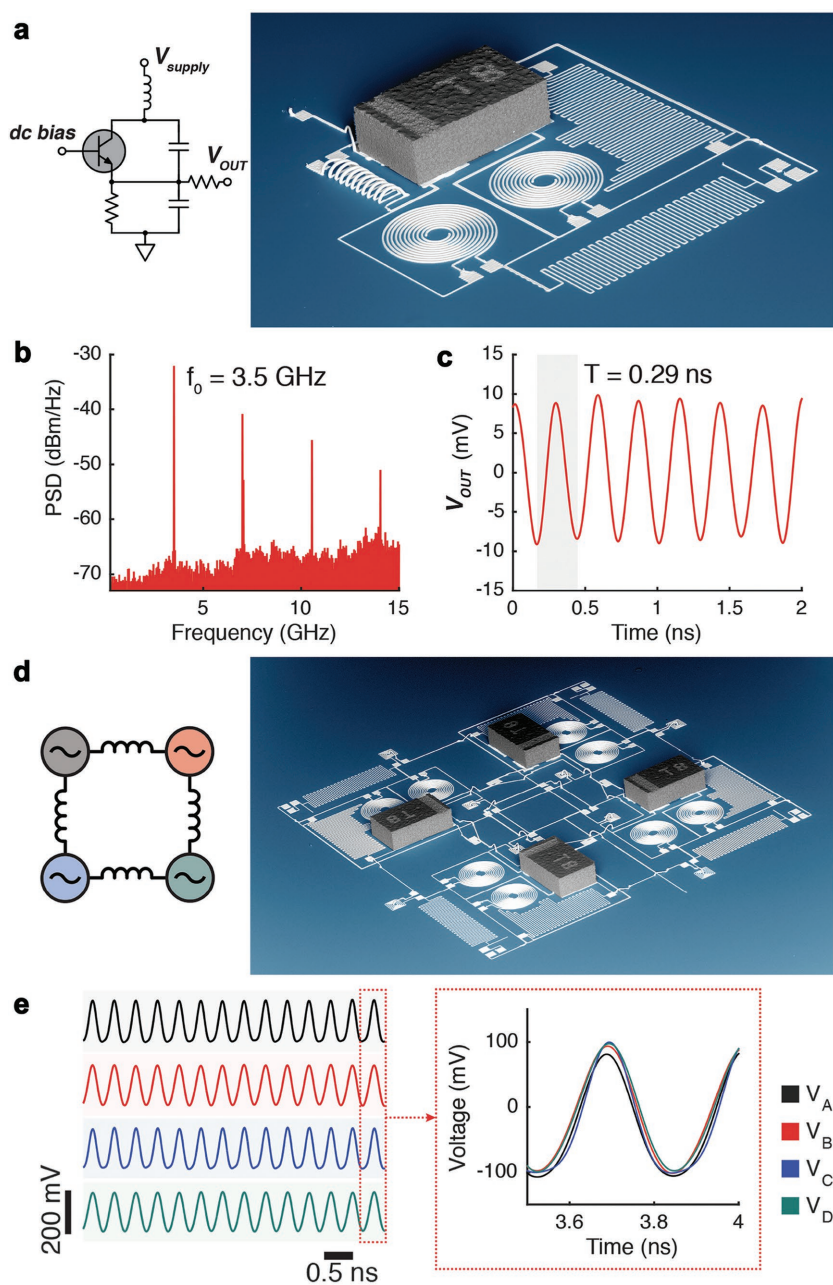


Figure 2. Lumped self-sustained oscillators and their synchronization network. a–c) A Colpitts oscillator with a 3D printed LC resonator, and its measured PSD and time-domain signal. d,e) An array of four injection-locked Colpitts oscillators and their measured time-domain signals. Each transistor in parts (a) and (d) has a footprint of 1 mm × 0.6 mm. Absolute time reference points in parts (c) and (e) are arbitrary. The power consumption of each Colpitts oscillator in parts (a) and (d) is ≈8 mW.

(Movie S4, Supporting Information). The printed silver passive features are heated at 300 °C for ≈30 min to enhance their conductivity after the transistor placement, with no deleterious effects of transistor performance observed. The oscillation frequency f_0 approximates the resonance frequency f_R of the LC resonator, with the discrepancy arising from the parasitic capacitance in the circuit. When the energy stored in the LC resonator is small, the transistor provides a gain larger than the

resonator loss, thus increasing the energy in the resonator. When the energy in the resonator exceeds a certain threshold, the nonlinearity of the transistor limits the gain. In this way, the circuit autonomously breaks into an oscillation starting from ambient noise, eventually reaching a self-sustained, steady-state oscillation at 3.5 GHz (Figure 2b,c), during which gain balances loss overall in each oscillation cycle. The linewidth of the oscillation power spectral density (PSD) (Figure 2b) is many orders of magnitude smaller than the linewidth of passive resonances (Figure 1). This linewidth narrowing is a hallmark signature of self-sustained oscillation. The small, yet nonvanishing, linewidth despite the self-sustenance of oscillation is due to noise perturbation.^[28] Note that while the DC resistance per unit cross-sectional area of the silver ink trace is ≈6 times larger than that of bulk silver, the DC voltage drop across the solenoidal inductor in the Colpitts oscillator is only 0.05 V, and hence, the use of the silver ink does not cause any appreciable issue for biasing the circuit (in fact, the circuit can tolerate the DC voltage drop as large as 0.2 V; see Figure S14 in the Supporting Information). Additional embodiments of Colpitts oscillators with different oscillation frequencies and substrates are provided in Figure S13 and S15 (Supporting Information).

We then created an array of four coupled Colpitts oscillators with injection locked synchronization (Figure 2d; Figure S16 and Movie S5, Supporting Information), since injection locking and synchronization generally play an important role in frequency synthesis and phase control in many wireless applications. We designed the four Colpitts oscillators to exhibit four slightly different oscillation frequencies of 3.01, 3.09, 3.17, and 3.22 GHz when uncoupled (Figure S17, Supporting Information), by introducing variations in L across the four LC resonators. Subsequently, we printed four 3.2 nH inductors to connect the emitter nodes of the transistors of adjacent oscillators (Figure S16, Supporting Information). These bridging inductors couple the oscillators via injection currents, leading to the injection locking of the four oscillators, with each oscillating at the same synchronized frequency of 3.10 GHz (Figure 2e). The size of the bridging inductance determines the coupling strength and influences the amplitude and phase of individual oscillators; with the 3.2 nH bridging inductance, the amplitude and phase do not exhibit appreciable variation among the four oscillators.

To attain self-sustained oscillations and their synchronizations from wave-based resonators, we differentially combined

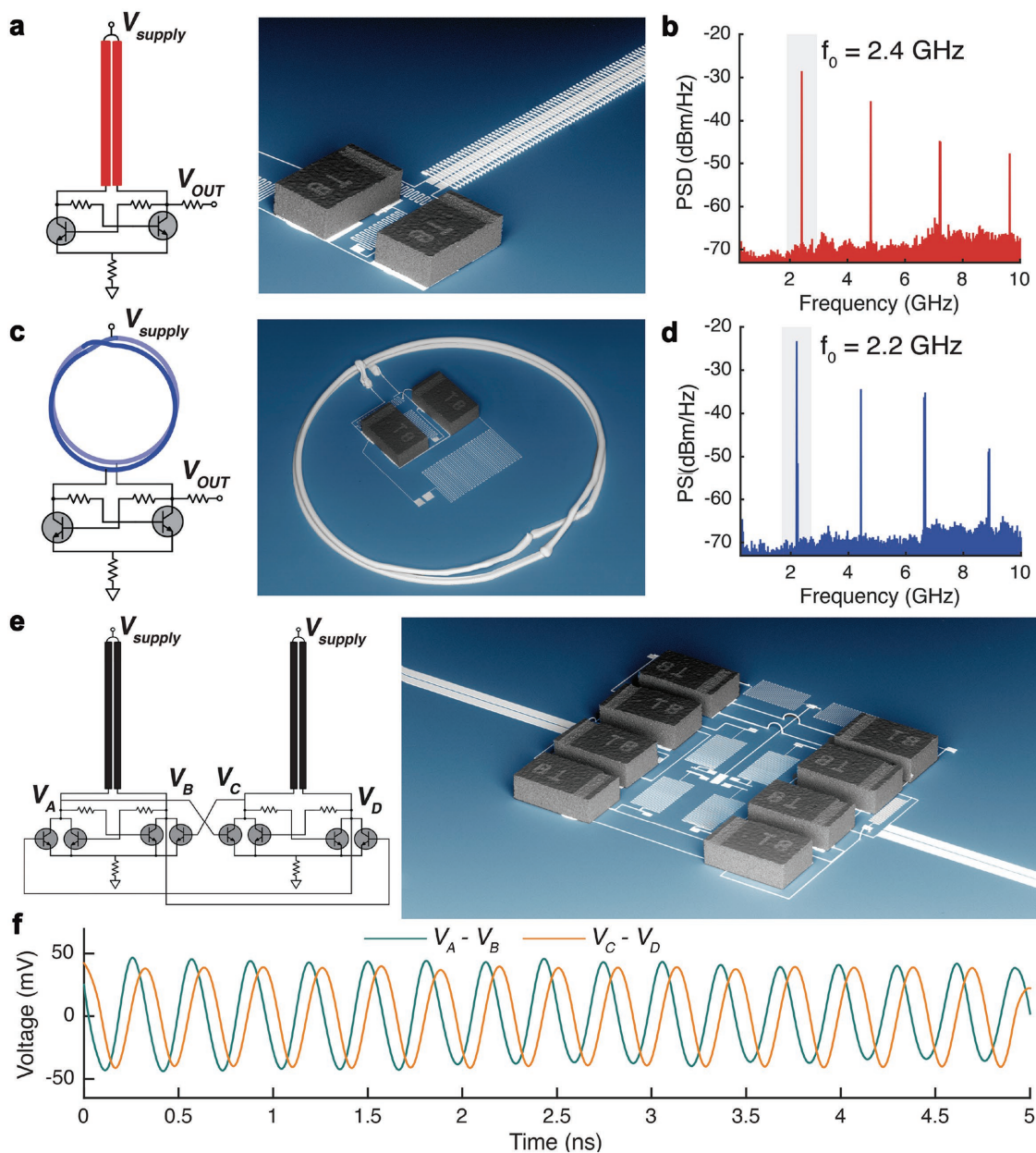


Figure 3. Self-sustained oscillators with wave-based resonators and their synchronization network. a,b) An oscillator combining a 4.2 mm long FMS-loaded CPS SWR with transistors, and its measured PSD. c,d) An oscillator combining a 5 mm diameter CPS Möbius ring with transistors and its measured PSD. e,f) Injection-locked quadrature oscillators with 6 mm long FMS-free CPS SWRs and their measured time-domain signals. Each transistor in parts (a), (c), and (e) has a footprint of 1 mm × 0.6 mm. The power consumption of each oscillator in parts (a), (c), and (e) is ≈18, ≈14, and ≈42 mW, respectively.

an FMS-loaded CPS SWR ($l = 4.2$ mm) with a pair of cross-coupled bipolar junction transistors at the open end of the CPS (Figure 3a).^[25] The cross-coupled transistors provide a gain that compensates the loss on the CPS SWR. The PSD and time-domain signal measured at one of the two symmetric collector terminals confirm a self-sustained 2.4 GHz oscillation (Figure 3b). This oscillation frequency is much smaller than the $\lambda/4$ standing wave resonance frequency (10.4 GHz) of the stand-alone CPS SWR because the quasi-TEM wave traveling back and forth on the CPS interacts with the substantial

parasitic capacitance from the transistors (see Experimental Section for a detailed theoretical analysis). Since these are single-ended measurements, the common mode signal is not nulled, manifesting as even-order harmonics (Figure 3b; Figure S18, Supporting Information). In another example, a similar differential combination of cross-coupled transistors with a 3D printed Möbius CPS ring yields a self-sustained 2.2 GHz oscillation (Figure 3c,d; Figure S18, Supporting Information). Note that the transistors are connected to the CPS in the ring position opposite to the Möbius twist. In yet another

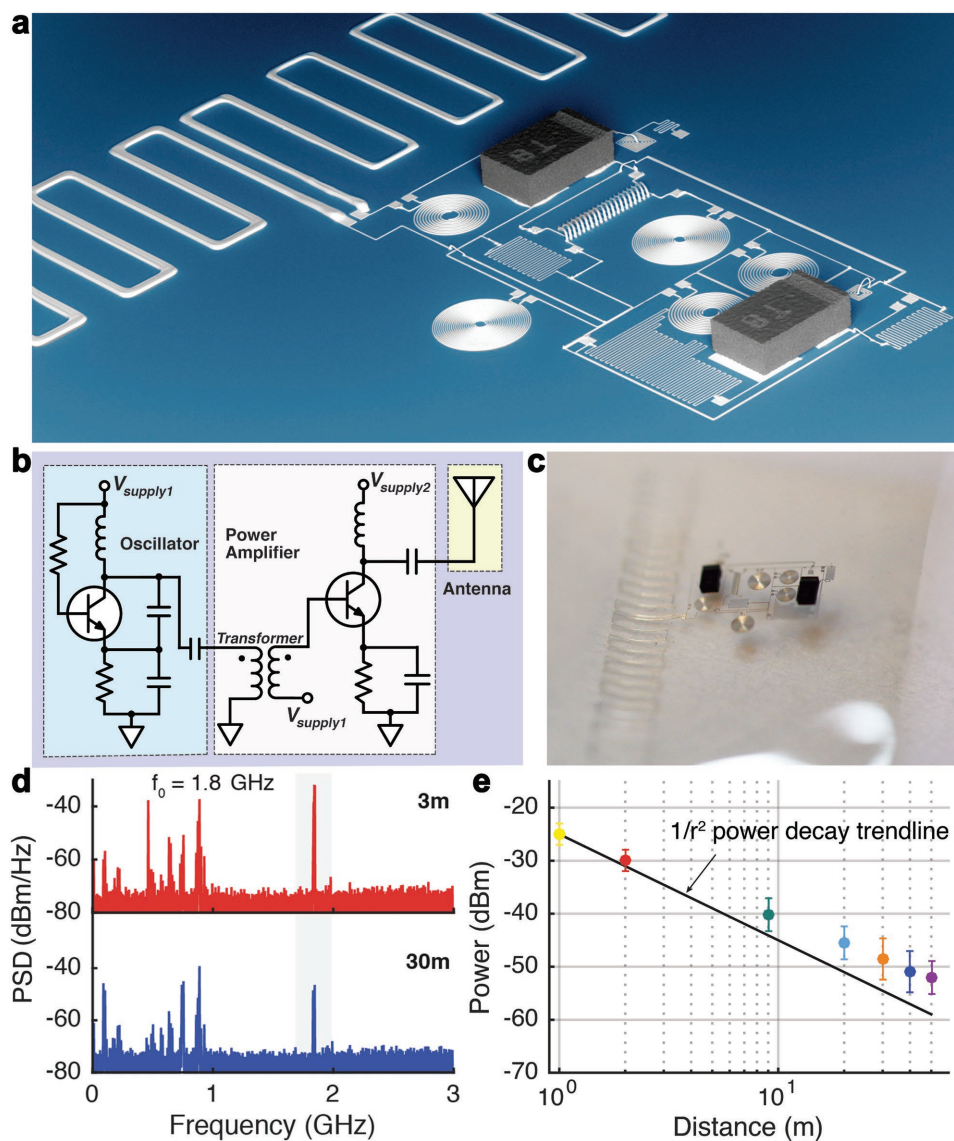


Figure 4. Wireless transmitter clocked by oscillator. a–c) 1.8 GHz RF transmitter on a) glass and c) polyimide substrates. Each transistor shown has a footprint of 1 mm × 0.6 mm. The total power consumption of each transmitter in parts (a) and (c) is ≈72 mW. d) PSD measured 3 and 30 m away from the transmitter on polyimide substrate. e) 1.8 GHz power (colored dots) versus distance from the transmitter, up against the theoretical inverse square law.

example, by coupling two oscillators similar to Figure 3a, but with more complex transistor networks, we once again produce an oscillator network that achieves synchronization via injection locking (Figure 3e and Movie S6, Supporting Information). Not only do these two oscillators injection lock to an identical oscillation frequency of 3.2 GHz, but they also lock in phase with an almost 90° phase difference due to the active coupling network,^[29] generating approximately quadrature (sine and cosine) signals (Figure 3f and Figure S18, Supporting Information). Since quadrature oscillators enable phase-sensitive heterodyning and image rejection, they play a pivotal role in many wireless systems.

As a final demonstration, we produce a 1.8 GHz RF transmitter clocked by a Colpitts oscillator (Figure 4a–c) on both glass and polyimide substrates. The oscillator drives a printed

meander dipole antenna through a class-A power amplifier. The power amplifier is also constructed by heterogeneously integrating the 3D printed passives with a bipolar junction transistor. The interface between the oscillator and the power amplifier is a 1:1 transformer, which provides DC isolation between the two functional blocks while affording an efficient AC transmission between them. The dipole antenna consists of two symmetrical arms, with each arm featuring meandered silver ink trace. By setting the total length of the two arms at $\lambda/2$ of 1.8 GHz, we obtain an optimal transmission with a radiation resistance of 35 Ω (Figure S19, Supporting Information). Figure 4d shows the PSD measured 3 and 30 m away from the transmitter (on the polyimide substrate) using a receiver antenna (APEX II—Hinged TG.35 Ultra-Wideband 4G LTE antenna) feeding a spectrum analyzer; the PSD measured at

1.8 GHz is the radiation from the transmitter, as it decreases with the increased distance and vanishes when the transmitter is turned off. By contrast, the PSDs measured below 1 GHz are spurious signals from environment and persist even when the transmitter is turned off. We repeat this measurement, varying the distance between the transmitter and the receiver from 1 to 50 m, and the power received at 1.8 GHz approximates the inverse square law (Figure 4e).

In summary, we have shown that a broad array of RF passive devices can be created by directly writing silver-nanoparticle inks both in-plane and out-of-plane. We further showed that these printed passive structures can be integrated with discrete transistors to attain RF electronic circuits, including self-sustained oscillators, injection-locked and synchronized oscillator arrays, and RF transmitters clocked by such oscillators. Our approach would also enable RF passives to be printed directly on complementary metal-oxide-semiconductor (CMOS) chips for rapid prototyping and testing of new device designs. We ultimately envision creating more complex passive electromagnetic structures, e.g., metamaterials,^[30] by co-printing multiple functional materials of varying magnetic, dielectric, and conductive properties. Diverse RF functionalities with improved passive performance should be realized by exploiting their 3D structure–function relation coupled with tailoring their composition locally.

Experimental Section

Ink Synthesis: Silver-nanoparticle inks were synthesized following the method reported previously.^[14] A solution containing 2 g of poly(acrylic acid) (PAA) (50 wt% polymer in water, molecular weight = 5000 g mol⁻¹), 1 g of PAA (25 wt% polymer in water, molecular weight = 50 000 g mol⁻¹), 40 g of diethanolamine, and 50 mL of deionized (DI) water was prepared. A separate solution was prepared by dissolving 20 g of AgNO₃ in 20 mL of DI water. These two solutions were mixed and stirred for 24 h at room temperature, followed by stirring for 2 h at 125 °C. The resulting silver-nanoparticle ink was concentrated by titrating with 300 mL of ethanol. Because ethanol is a poor solvent for the PAA-coated silver nanoparticles, rapid coagulation ensued. After decanting the supernatant, the coagulated ink was centrifuged at 9000 rpm for 20 min to remove excess solvent and recover the precipitate. This precipitate was re-dispersed in 20 mL of DI water and filtered through a 5 µm syringe filter (Millipore). The filtered solution was titrated with 60 mL of ethanol for precipitation of silver nanoparticles. After decanting the supernatant once again, the coagulated ink was further centrifuged at 5000 rpm for 20 min and the precipitate was collected. The final step of silver-nanoparticle ink synthesis involved homogenization at 2000 rpm and de-airing for ≈2 h under a light vacuum (≈847 mbar).

3D Printing: Direct ink writing was carried out using a 3-axis micropositioning stage (ABL 900010, Aerotech, Inc., Pittsburgh, PA, USA), whose motion was controlled by computer-aided design software (RoboCAD, 3D Inks, Stillwater, OK, USA). The silver ink was housed in a syringe (3 mL barrel, EFD Inc., East Providence, RI, USA) attached by Luer-Lock to a borosilicate micronozzle (diameter = 5, 10, and 50 µm produced using a P-2000 micropipette puller, Sutter Instrument Co., Novato, CA, USA). An air-powered fluid dispenser (800 ultradispensing system, EFD Inc.) and a high-pressure adapter were used to pressurize the barrel and to control the ink flow rate. The typical pressure value required for direct ink writing ranges from 100 to 250 psi for a printing speed of 50–500 µm s⁻¹. Omnidirectional printing was performed in air under ambient conditions with a relative humidity of 35–50% and a temperature of 23–26 °C on either glass (Corning 1737 AMLCD glass) or flexible polyimide substrate (Dupont Kapton PV9103).

All the electromagnetic components were printed using 10 µm nozzles, except the meander dipole antenna and Möbius and simple CPS rings, which were printed using 50 µm nozzles. Interconnects were printed using 10 µm nozzles, while the resistors were printed using 5 or 10 µm nozzles to enhance trace resistance. The printed passives were sintered typically at 300 °C for 30 min to obtain an electrical resistivity of ≈1 × 10⁻⁵ Ω cm. Over a longer time (3–4 weeks), the resistivity slowly increases due to oxidation, which can be reversed by heating at 300 °C for 15–20 min. Using a 10 µm diameter nozzle, the material cost for printing a 1 m long interconnect was estimated to be 0.4 cents. Three examples of passive electromagnetic component printing are described in more detail below.

To fabricate the 1:1 transformer, first twenty 200 µm long bars with a bar width of 10 µm and a bar-to-bar spacing of 40 µm were printed onto the substrate. Then, out-of-plane printing of semicircles was performed with a diameter of ≈220 µm to connect alternate bars. This created two mutually interpenetrating solenoidal inductors that form the 1:1 transformer. The printing of the 3:1 transformer (Figure S1d, bottom, Supporting Information) was done in a similar manner, but by first printing two different lengths of bars (200 and 300 µm) alternately in a number ratio of 3:1. The primary and secondary solenoidal coils were subsequently constructed by printing small out-of-plane semicircles with a diameter of 210–220 µm, then large out-of-plane semicircles with a diameter of ≈360 µm.

To fabricate the FMS-loaded CPS, first two silver conductor lines constituting a CPS were printed. A high-viscosity polystyrene (PS) ink, prepared by dissolving 2 g of PS (molecular weight = 2 000 000 g mol⁻¹; Pressure Chemical, PS61111) in 2 g of toluene (Sigma-Aldrich), was then printed using a 10 µm nozzle directly above the CPS (Scheme S1b, Supporting Information). Above this PS sacrificial layer, 200 µm long FMSs were printed in a direction perpendicular to the CPS length; each FMS had a width of 10 µm and the inter-FMS spacing was 40 µm. Volumetric shrinkage of silver-nanoparticle ink that would occur in the later sintering step was precompensated during FMS printing; concretely, curved FMSs with a radius of curvature of 300 µm were printed, as they would be shrunken and deformed to approximate intended linear FMSs after sintering. An example of FMS-loaded CPS printing can be found in Movie S2 (Supporting Information). After a light sintering at 200 °C for 10 min, the structure was immersed in toluene for 10 min to dissolve and remove the PS layer. The final structure was then once again sintered at 300 °C for 30 min.

To fabricate the Möbius CPS ring, first a silver ink split ring was printed using a 50 µm glass nozzle. A sacrificial PS layer was printed using a 50 µm glass nozzle on top of the split ring. Subsequently, another silver ink ring was printed on top of the PS layer, which was connected to the bottom ring at its split portion in the way that the characteristic twist of the Möbius ring was created. An example of Möbius ring printing can be found in Movie S3 (Supporting Information). The resulting Möbius ring structure was lightly sintered at 200 °C for 10 min, followed by immersion in toluene for 10 min to dissolve and remove the PS layer. Another step of sintering was taken at 300 °C for 30 min. Two pads that constitute an RF measurement port were printed at a ring site opposite to the Möbius twist, with one pad connected to the bottom ring and the other pad connected to the top ring. In the Möbius ring oscillator (Figure 3c), the cross-coupled bipolar junction transistors were connected to this RF measurement port.

Hybrid Integration of Printed Passive Devices and Transistors: The construction of the oscillators and transmitters was achieved by placing surface-mount bipolar junction transistors (Infineon BFR840L3RHESD) in the appropriate positions in the 3D printed passive structures. Specifically, the transistors were picked and placed using a 200 µm plastic nozzle (Part 7018417, Nordson EFD) on the micropositioning stage by applying a modest vacuum (18 psi; Movie S4, Supporting Information). The position control was done automatically; the orientation control was done manually. For these heterogeneously integrated circuits, the sintering step at 300 °C for 30 min was performed after the transistors were placed, with no malfunction of the transistor being observed after the sintering.

Design and Characterization of Passive Electromagnetic Components: An electromagnetic field solver, Sonnet, was used to design the variety of passive electromagnetic components shown in Figure 1 and Figure S1–S5 (Supporting Information); see Figure S6–S8 (Supporting Information), for example, for simulation results. Printed components were characterized in the frequency range of 45 MHz to 50 GHz by microwave scattering analysis using an Agilent E8364A PNA vector network analyzer. Measurements were carried out on a probe station equipped with two signal-ground microwave probes with each probe having a 150 μm pitch. The measurement setup was calibrated to the probe tips using calibration software (Cascade Microtech WinCal XE) and a short-open-load-thru impedance standard substrate.

1-port scattering analysis was used for the inductors, capacitors, LC resonators, CPS SWRs, and CPS Möbius and simple ring resonators. From the measured scattering parameter s_{11} —which is equivalent to the reflection coefficient at the measurement port—the input impedance Z_{in} of the device under test was obtained through the following relation:

$$Z_{in} = Z_m \frac{1 + s_{11}}{1 - s_{11}} \quad (1)$$

where $Z_m = 50 \Omega$ is the impedance of the measurement system. Z_{in} as a function of frequency directly revealed the resonant behaviors of the LC and CPS resonators, whereas L , C , and Q values for stand-alone inductors and capacitors were extracted from the measured Z_{in} versus frequency according to the following formulae:

$$L = \frac{\text{Im}[Z_{in}]}{\omega} \quad (2)$$

$$Q = \frac{\text{Im}[Z_{in}]}{\text{Re}[Z_{in}]} \text{ (inductor quality factor)} \quad (3)$$

$$C = -\frac{\text{Im}[Z_{in}]^{-1}}{\omega} \quad (4)$$

$$Q = -\frac{\text{Im}[Z_{in}]}{\text{Re}[Z_{in}]} \text{ (capacitor quality factor)} \quad (5)$$

where ω is the angular frequency. In this extraction process, the inductors and capacitors were modeled as series R - L and R - C networks, respectively, as the loss in these insulating substrates was negligible, obviating the need for shunt conductance in the model.

Two-port microwave scattering measurements were performed to characterize the transformers, where four scattering parameters s_{11} , s_{12} , s_{21} , and s_{22} were measured. Then, these measured s -parameters were converted into Z -parameter,^[31] from which the coupling coefficient k and power transfer efficiency P_{out}/P_{in} of the transformer were evaluated according to the following formulae:

$$k = \frac{\text{Im}[Z_{21}]}{\sqrt{\text{Im}[Z_{11}] \cdot \text{Im}[Z_{22}]}} \quad (6)$$

$$\frac{P_{out}}{P_{in}} = \frac{|s_{21}|^2 / Z_0}{\text{Re}[|s_{11} + 1|^2 / Z_{in}]} \quad (7)$$

Design and Characterization of Self-Sustained Oscillators: The self-sustained oscillators (Figure 2 and 3) were designed using the circuit simulator in Cadence, a computer-aided tool for circuit design, layout, and verification. For these simulations, vendor-provided Spice models were used for the bipolar junction transistors and measured s -parameters for the RF passive electromagnetic components.

The LC lumped oscillator of Figure 2a (see also Figure S13 in the Supporting Information) adopts the Colpitts topology. The oscillation

frequency f_0 is approximately the resonant frequency f_R of the LC tank—which was the series combination of the two capacitors in parallel with the inductor—with the difference between f_0 and f_R arising from the parasitic capacitance in the circuit. The oscillator's output signal was measured at the transistor's emitter node, but through a printed 80 Ω series resistor that mitigated the loading of the oscillator by the 50 Ω impedance of the measurement systems (Agilent's E4448A PSA spectrum analyzer and Infiniium 54855A oscilloscope). For the injection locked oscillator array (Figure 2d), slight variations in the size of the LC tank inductors were implemented so that the four constituent Colpitts units had four slightly different oscillation frequencies of 3.01, 3.09, 3.17, and 3.22 GHz when uncoupled (Figure S17, Supporting Information). When coupled via four 3.2 nH bridging inductors, the four oscillators locked at the same frequency. In the design of the oscillators with wave-based resonators (Figure 3; see also Figure S18 in the Supporting Information), 80 Ω resistors inserted between the base and collector nodes of cross-coupled transistors increased the oscillation amplitude. The oscillator output was measured at the transistor's collector nodes but once again after 80 Ω printed series resistors to mitigate loading by the measurement systems.

Design and Characterization of RF Transmitters: The transmitter (Figure 4; see also Figure S19a in the Supporting Information) consists of three major functional blocks, a Colpitts oscillator, a class-A power amplifier, and a meander dipole antenna: the oscillator generates an RF signal, which the power amplifier uses to drive the antenna. The target design frequency is ≈1.8 GHz in the cellular communication band. The 1:1 transformer inserted between the oscillator and the power amplifier provides DC blocking and AC coupling. The meander dipole antenna was designed to resonate at the target design frequency of 1.8 GHz (Figure S19b,c, Supporting Information). The antenna was characterized by measuring its s -parameter in 1-port microwave scattering analysis with the Agilent E8364A PNA vector network analyzer (Figure S19c, Supporting Information) and imported these measurement-based antenna characteristics to the Cadence circuit simulator in order to simulate the complete transmitter. The RF transmission of the implemented circuit was characterized outdoors (Figure 4). The transmitted signal was picked up by a commercial antenna (Apex II—Hinged TG.35 Ultra-Wideband 4G LTE antenna) connected to an Agilent E4448A PSA spectrum analyzer. The signal was detectable at least up to 50 m.

Theoretical Analysis: The considerable discrepancy between the oscillation frequency $f_0 \approx 2.4$ GHz of the oscillator combining the CPS SWR ($l = 4.2$ mm) and transistors (Figure 3a) and the fundamental resonance frequency $f_R \approx 10.4$ GHz of the CPS SWR (Figure 1k) can be understood as follows. The input impedance Z_{in} of the CPS SWR (Figure S20a, left, Supporting Information) is given by $Z_{in} = iZ_0 \tan(\beta l)$, where $\beta = 2\pi/\lambda$ is the wavenumber and Z_0 is the CPS's characteristic impedance. This β -dependent Z_{in} is due to the superposition of incident and reflected waves. At frequencies where $\beta l = n \times \pi/2$ or $l = n \times \lambda/4$ (where n is an integer), $|Z_{in}|$ becomes maximum (odd n) or minimum (even n) (Figure S20a, right, Supporting Information). These corresponded to standing wave resonance modes. The fundamental mode at $\beta l = \pi/2$ or $l = \lambda/4$ ($n = 1$) sets f_R . On the other hand, in the oscillator, the CPS SWR was loaded by parasitic capacitance C_{tran} of the transistors (Figure S20b, left, Supporting Information), creating a new effective passive network with $Z_{in} = (i\omega C_{tran})^{-1} || iZ_0 \tan(\beta l)$. The fundamental resonance mode of this new passive network, which sets f_0 , occurs at the smallest βl that maximizes $|Z_{in}|$. In general, the maximum $|Z_{in}|$ occurs when βl satisfies:

$$\frac{1}{\beta l} \times \frac{l}{\nu C_{tran} Z_0} = \tan(\beta l) \quad (8)$$

where ν is the wave velocity. The βl solutions for Equation (8) occur when the two functions of βl on the left- and right-hand sides of Equation (8) intersect (Figure S20b, right, Supporting Information). As seen, the smallest βl solution (corresponding to f_0) was smaller than $\beta l = \pi/2$ (corresponding to f_R). This was the physical origin of $f_0 < f_R$ observed in this work.

Supporting Information

Supporting Information is available from the Wiley Online Library or from the author.

Acknowledgements

N.Z. and C.L. contributed equally to this work. The authors thank James Weaver and Lori Sanders for their assistance with image preparation and photography, and Prof. Hanjun Jiang and Dr. Ling Qin for invaluable scientific discussions and assistance with design. The authors are grateful for the support of this research by the U.S. Department of Energy through its Energy Frontier Research Center, Light–Material Interactions in Energy Conversion (DE-SC0001293). N.Z. thanks the Camille and Henry Dreyfus Foundation for a Postdoctoral Fellowship in Environmental Chemistry. D.H. acknowledges the Army Research Office (W911NF-15-1-0565).

Received: September 26, 2016
Published online:

-
- [1] B. K. Tehrani, B. S. Cook, M. M. Tentzeris, *IEEE Antennas Wireless Propag. Lett.* **2016**, *15*, 143.
- [2] G. McKerricher, J. G. Perez, A. Shamim, *IEEE Trans. Electron Devices* **2015**, *62*, 1002.
- [3] A. Bisognin, J. Thiellex, W. Wei, D. Titz, F. Ferrero, P. Brachat, G. Jacquemod, H. Happy, C. Luxey, *IEEE Antennas Wireless Propag. Lett.* **2014**, *13*, 435.
- [4] H. Subbaraman, D. T. Pham, X. Xu, M. Y. Chen, A. Hosseini, X. Lu, R. T. Chen, *IEEE Antennas Wireless Propag. Lett.* **2013**, *12*, 170.
- [5] L. Yang, A. Rida, R. Vyas, M. M. Tentzeris, *IEEE Trans. Microwave Theory Tech.* **2007**, *55*, 2894.
- [6] D. Redinger, S. Moles, S. Yin, R. Farschi, V. Subramanian, *IEEE Trans. Electron Devices* **2004**, *51*, 1978.
- [7] J. R. Corea, A. M. Flynn, B. Lechêne, G. Scott, G. D. Reed, P. J. Shin, M. Lustig, A. C. Arias, *Nat. Commun.* **2016**, *7*, 10839.
- [8] A. E. Ostfeld, I. Deckman, A. M. Gaikwad, C. M. Lochner, A. C. Arias, *Sci. Rep.* **2015**, *5*, 15959.
- [9] A. Martínez-Olmos, J. Fernández-Salmerón, N. Lopez-Ruiz, A. R. Torres, L. F. Capitan-Vallvey, A. J. Palma, *Anal. Chem.* **2013**, *85*, 11098.
- [10] Y. Kim, H. Kim, H.-J. Yoo, *IEEE Trans. Adv. Packag.* **2010**, *33*, 196.
- [11] A. E. I. Lamminen, J. Säily, A. R. Vimpari, *IEEE Trans. Antennas Propag.* **2008**, *56*, 2865.
- [12] H. Kang, H. Park, Y. Park, M. Jung, B. C. Kim, G. Wallace, G. Cho, *Sci. Rep.* **2014**, *4*, 5387.
- [13] R. Sorrentino, O. A. Peverini, *Proc. IEEE* **2016**, *104*, 1362.
- [14] B. Y. Ahn, E. B. Duoss, M. J. Motala, X. Guo, S.-I. Park, Y. Xiong, J. Yoon, R. G. Nuzzo, J. A. Rogers, J. A. Lewis, *Science* **2009**, *323*, 1590.
- [15] C. Ladd, J.-H. So, J. Muth, M. D. Dickey, *Adv. Mater.* **2013**, *25*, 5081.
- [16] J. Hu, M.-F. Yu, *Science* **2010**, *329*, 313.
- [17] J. J. Adams, E. B. Duoss, T. F. Malkowski, M. J. Motala, B. Y. Ahn, R. G. Nuzzo, J. T. Bernhard, J. A. Lewis, *Adv. Mater.* **2011**, *23*, 1335.
- [18] M. S. Mannoor, Z. Jiang, T. James, Y. L. Kong, K. A. Malatesta, W. O. Soboyejo, N. Verma, D. H. Gracias, M. C. McAlpine, *Nano Lett.* **2013**, *13*, 2634.
- [19] M. Liang, W.-R. Ng, K. Chang, K. Gbele, M. E. Gehm, H. Xin, *IEEE Trans. Antennas Propag.* **2014**, *62*, 1799.
- [20] H. Yi, S.-W. Qu, K.-B. Ng, C. H. Chan, X. Bai, *IEEE Trans. Antennas Propag.* **2016**, *64*, 442.
- [21] S. Kim, A. Shamim, A. Georgiadis, H. Aubert, M. M. Tentzeris, *IEEE Trans. Compon. Packag., Manuf. Technol.* **2016**, *6*, 486.
- [22] O. A. Peverini, G. Addamo, R. Tascone, G. Virone, P. Cecchini, R. Mizzone, F. Calignano, E. P. Ambrosio, D. Manfredi, P. Fino, *IEEE Trans. Microwave Theory Tech.* **2015**, *63*, 3361.
- [23] A. Ruaro, J. Thaysen, K. B. Jakobsen, *IEEE Trans. Antennas Propag.* **2016**, *64*, 2127.
- [24] A. Macor, E. de Rijk, S. Alberti, T. Goodman, J.-Ph. Ansermet, *Rev. Sci. Instrum.* **2012**, *83*, 046103.
- [25] W. F. Andress, D. Ham, *IEEE J. Solid-State Circuits* **2005**, *40*, 638.
- [26] D. Ham, W. Andress, in *2004 IEEE International Solid-State Circuits Conference*, IEEE, Piscataway, NJ, USA **2004**, p. 380, DOI: 10.1109/ISSCC.2004.1332753.
- [27] D. J. Ballon, H. U. Voss, *Phys. Rev. Lett.* **2008**, *101*, 247701.
- [28] D. Ham, A. Hajimiri, *IEEE J. Solid-State Circuits* **2003**, *38*, 407.
- [29] A. Mirzaei, M. E. Heidari, R. Bagheri, S. Chehrizi, A. A. Abidi, *IEEE J. Solid-State Circuits* **2007**, *42*, 1916.
- [30] H. Yoon, K. Y. M. Yeung, V. Umansky, D. Ham, *Nature* **2012**, *488*, 65.
- [31] D. M. Pozar, *Microwave Engineering*, Wiley, Hoboken, NJ, USA **2011**.
-